

# A Chemical Route to Monolithic Integration of Crystalline Oxides on Semiconductors

Martin D. McDaniel, Thong Q. Ngo, Agham Posadas, Chengqing Hu, Sirong Lu, David J. Smith, Edward T. Yu, Alexander A. Demkov, and John G. Ekerdt\*

This work demonstrates the growth of crystalline SrTiO<sub>3</sub> (STO) directly on germanium via a chemical method. After thermal deoxidation, the Ge substrate is transferred in vacuo to the deposition chamber where a thin film of STO (2 nm) is deposited by atomic layer deposition (ALD) at 225 °C. Following post-deposition annealing at 650 °C for 5 min, the STO film becomes crystalline with epitaxial registry to the underlying Ge (001) substrate. Thicker STO films (up to 15 nm) are then grown on the crystalline STO seed layer. The crystalline structure and orientation are confirmed via reflection high-energy electron diffraction, X-ray diffraction, and transmission electron microscopy. Electrical measurements of a 15-nm thick epitaxial STO film on Ge show a large dielectric constant ( $k \approx 90$ ), but relatively high leakage current of  $\approx 10$  A/cm<sup>2</sup> for an applied field of 0.7 MV/cm. To suppress the leakage current, an aluminum precursor is cycled during ALD growth to grow crystalline Al-doped STO (SrTi<sub>1-x</sub>Al<sub>x</sub>O<sub>3-δ</sub>) films. With sufficient Al doping ( $\approx 13\%$ ), the leakage current decreases by two orders of magnitude for an 8-nm thick film. The current work demonstrates the potential of ALD-grown crystalline oxides to be explored for advanced electronic applications, including high-mobility Ge-based transistors.

## 1. Introduction

The monolithic integration of crystalline oxides on silicon was first reported by McKee and co-workers in 1998.<sup>[1]</sup> Since that initial work, several research groups have been extensively involved in studying the growth of crystalline oxides integrated

on semiconductors.<sup>[2-10]</sup> Recently, epitaxial oxide heterostructures have been studied to explore interface phenomena, such as superconductivity, magneto-electric coupling, and quantum Hall effect.<sup>[11-17]</sup> A wide-array of properties, in combination with monolithic integration on semiconductors, make crystalline oxides attractive candidates for next-generation electronic devices. Molecular beam epitaxy (MBE) has been the dominant method for growth on silicon due to the layer-by-layer growth mode and precise oxygen control, which prevents formation of an amorphous interfacial layer (e.g., SiO<sub>2</sub>) under appropriate conditions.<sup>[6-8]</sup> However, for industrial applications, atomic layer deposition (ALD) has advantages over MBE primarily due to its conformal coverage, low thermal budget, scalability, and cost.<sup>[18,19]</sup>

Over the last several decades, silicon has been the workhorse for the semiconductor industry, because of its high-quality oxide SiO<sub>2</sub>. More recently, device

scaling to smaller feature sizes in complementary metal-oxide-semiconductor (CMOS) technology has led to the development of high-*k* dielectrics to replace the traditional SiO<sub>2</sub> gate oxide due to unacceptably high leakage current in ultrathin (<1 nm) SiO<sub>2</sub>.<sup>[20,21]</sup> High-*k* dielectrics (e.g., HfO<sub>2</sub>) allow for thicker gate oxides to be used by a factor of  $k/3.9$ , and can therefore be used to reduce the leakage current. When using alternative high-*k* dielectric layers, the presence of any SiO<sub>2</sub> at the oxide-semiconductor interface lowers the effective gate capacitance, reducing the benefits of the high-*k* material.

Germanium exhibits higher hole and electron mobilities than silicon,<sup>[22]</sup> potentially enabling device operation at higher speed. The 2012 international technology roadmap for semiconductors (ITRS) expects the introduction of high-mobility channels by 2018.<sup>[23]</sup> When high-*k* dielectrics are desired, the chemical instability of GeO<sub>2</sub> versus SiO<sub>2</sub> may actually be an advantage. Integration of high-*k* dielectrics on germanium has been studied by several groups,<sup>[24-29]</sup> but the electrical performance of Ge-based devices has been less than optimal. Several methods have been employed to control the interface state density ( $D_{it}$ ) in order to achieve high performance.<sup>[27-29]</sup> Typical values reported for high-*k*/Ge gate stacks show  $D_{it} \approx 10^{11}-10^{12}$  cm<sup>-2</sup> eV<sup>-1</sup>. For practical realization of high-mobility channels in CMOS technology, surface passivation of the semiconductor substrate and

M. D. McDaniel, T. Q. Ngo, Prof. J. G. Ekerdt  
McKetta Department of Chemical Engineering  
The University of Texas at Austin  
Austin, TX 78712, USA  
E-mail: ekerdt@utexas.edu

Dr. A. Posadas, Prof. A. A. Demkov  
Department of Physics  
The University of Texas at Austin  
Austin, TX 78712, USA

C. Hu, Prof. E. T. Yu  
Department of Electrical and Computer Engineering  
The University of Texas at Austin  
Austin, TX 78758, USA

S. Lu, Prof. D. J. Smith  
Department of Physics  
Arizona State University  
Tempe, AZ 85287, USA



DOI: 10.1002/admi.201400081

a high-quality oxide-semiconductor interface must be realized. Previous work has shown that crystalline oxides on semiconductors have the potential to create a nearly perfect electrical interface by drastically reducing the interface trap density ( $D_{it} < 10^{10} \text{ cm}^{-2} \text{ eV}^{-1}$ ).<sup>[30]</sup>

To date, the majority of research on crystalline oxides integrated with semiconductors has been based on strontium titanate, SrTiO<sub>3</sub> (STO), epitaxially grown on Si (001) by MBE. Furthermore, many of the functional crystalline oxides and heterostructures integrated with Si have utilized an STO buffer layer.<sup>[31–38]</sup> Despite the promise of crystalline oxides on semiconductors, the lack of alternative growth methods has limited their study. Previous attempts to grow crystalline oxides directly on Si by chemical routes, including ALD, have been unsuccessful. In earlier work, we demonstrated a combined MBE-ALD growth technique, where a four-unit-cell STO buffer layer grown by MBE was required to provide a stable template for the growth of crystalline oxides by ALD on Si (001), including anatase TiO<sub>2</sub>, SrTiO<sub>3</sub>, BaTiO<sub>3</sub>, and LaAlO<sub>3</sub>.<sup>[39–42]</sup> Despite this success, a purely chemical route to integrating crystalline oxides on semiconductors is still lacking.

In this current work, we demonstrate the ability to grow a crystalline oxide, STO, directly on Ge (001) by ALD. After removing the native oxide of Ge under ultra-high vacuum conditions, the substrate is transferred *in vacuo* to the ALD chamber. Post-deposition annealing at 650 °C is required after the deposition, resulting in a crystalline STO film in epitaxial registry with the underlying Ge (001) substrate. Detailed structural and initial electrical characterization of epitaxial STO and Al-doped STO on Ge (001) is described.

## 2. Growth of Crystalline SrTiO<sub>3</sub> on Ge (001)

### 2.1. Preparation of the Ge (001) Surface

Before deposition of the STO film, the Ge (001) surface is prepared in an ultra-high vacuum (UHV) system with a base pressure below  $3 \times 10^{-9}$  torr. After solvent degreasing, the sample is dried and exposed to an ultraviolet/ozone unit to remove residual carbon contamination. The sample is moved directly into the UHV annealing chamber, equipped with a silicon carbide heater and reflection high-energy electron diffraction (RHEED). Thermal deoxidation of the Ge wafer is achieved by annealing the sample at a temperature 700 °C for 1 hr. A representative x-ray photoelectron spectrum of the Ge 3d feature (Supporting Information) illustrates the possible presence of Ge<sub>2</sub>O, accounting for 0.8% of the total Ge signal after annealing and transferring the sample into the analytical chamber. When the sample is cooled below 200 °C, the 2× reconstructed Ge (001) surface is observed by RHEED (not shown). The 2× reconstruction was also observed along the perpendicular surface direction by rotating the sample 90° under electron illumination. The intensity of the ½-order spots in the 2×1 surface reconstruction is a strong indicator of the quality of the cleaned Ge surface. In our previous work, thermal deoxidation of the Ge surface was achieved by using *in situ* oxygen plasma treatment followed by annealing at 650 °C or higher for 30 min, where the root-mean-square roughness over a  $5 \times 5 \mu\text{m}^2$  area

decreased from  $0.9 \pm 0.2$  nm when using a similar protocol to that employed for the study herein to  $0.3 \pm 0.1$  nm, respectively.<sup>[43]</sup> However, in this work, only the thermal deoxidation described above is used to prepare the Ge surface for ALD growth. We found that provided a reasonable 2× reconstruction was observed, crystalline STO film growth could be achieved.

### 2.2. Atomic Layer Deposition of Crystalline SrTiO<sub>3</sub>

After preparing the 2× reconstructed Ge (001) surface, the sample is transferred *in vacuo* from the annealing chamber to the ALD system. Thin film growth of STO on the thermally deoxidized Ge (001) substrate is achieved by ALD at a substrate temperature of 225 °C using strontium bis(triisopropylcyclopentadienyl) [Sr(<sup>i</sup>Pr<sub>3</sub>Cp)<sub>2</sub>] (HyperSr),<sup>[44]</sup> titanium tetraisopropoxide [Ti(O-<sup>i</sup>Pr)<sub>4</sub>] (TTIP),<sup>[45]</sup> and purified water as co-reactants. Both the Sr and Ti metalorganic precursors were chosen for this study due to their commercial availability and common use in ALD.<sup>[46–55]</sup>

As with the deposition of any ternary oxide by ALD, the “supercycle” consists of a combination of subcycles for the binary oxides. Each subcycle of Sr and Ti consists of a 2-sec dose of the metalorganic precursor, a 15-sec purge with Ar, a 1-sec pulse of H<sub>2</sub>O, and a final 15-sec purge with Ar. From our previous experience of growing STO on STO-buffered Si (001), Sr:Ti cycle ratios of 1:1 to 4:3 were needed to achieve nearly stoichiometric films.<sup>[40]</sup> However, the initial STO growth on Ge behaves differently. The STO nucleation on Ge uses a Sr-heavy supercycle (a ratio of 2 Sr subcycles to 1 Ti subcycle) to achieve stoichiometric to slightly Sr-rich STO films, which is critical to achieving an epitaxial crystalline film. Under these conditions, a thin amorphous STO film ( $\approx 2$  nm) is first deposited with 12 supercycles, equivalent to 36 subcycles.

The thin STO film on Ge is then transferred *in vacuo* back to the annealing chamber. The film is heated to a substrate temperature of 650 °C at a rate of 20 °C min<sup>-1</sup> for crystallization. The process flow for growth and crystallization of the STO layer on Ge (001) is shown schematically in **Figure 1**. The atomic model of the STO-Ge interface illustrated in **Figure 1** is only an elementary schematic, as the exact interface structure and bonding across the interface is not known at this time. Upon post-deposition annealing, the transition of the film from amorphous to crystalline is directly observed by the RHEED imaging system, as shown in **Figure 2**. After annealing, the sample is cooled to below 200 °C. Further growth on the crystalline STO-Ge heterostructure is then possible. The detailed mechanism of the initial nucleation of STO on the Ge (001) surface is not yet completely understood. The clean Ge (001) surface that is transferred into the ALD system is without surface hydroxyl groups, which are the presumed reaction sites for these ALD precursors. Interestingly, initial growth analysis of the two binary oxides, SrO and TiO<sub>2</sub>, suggests that the Sr precursor (HyperSr) reacts with the Ge (001) surface to initiate film nucleation. Using only the Ti precursor (TTIP), no film deposition was observed even after 100 ALD subcycles. Considering the structure of the cyclopentadienyl-based precursor compared with the alkoxide, the nucleation process may result more from direct chemical bonding between the electropositive

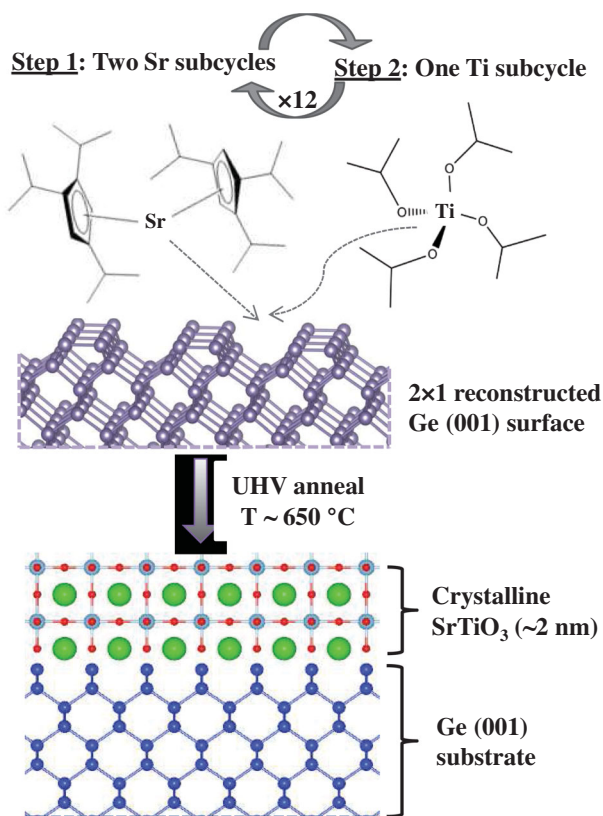


**Figure 1.** Schematic of the nucleation process for STO on Ge (001) by ALD. The deposition subcycle includes the H<sub>2</sub>O exposure and argon purge steps.

Sr and the empty dangling bond states on the Ge (001) surface. A more detailed study of the cyclopentadienyl-based precursor interaction with the Ge surface is beyond the scope of this current work.

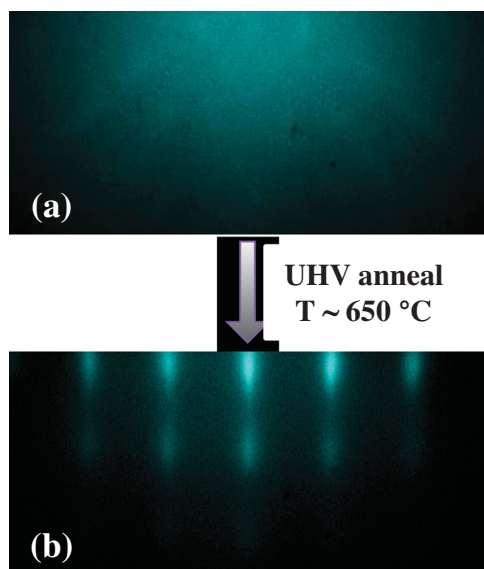


**Figure 2.** RHEED images (a) after  $\approx 2$  nm STO film growth by ALD (36 subcycles) and (b) after vacuum annealing at 650 °C, where the beam is aligned along the [110] azimuth.

### 2.3. Thicker Oxide Film Growth

For thicker STO films, the crystallized STO on Ge was transferred back into the ALD chamber, following the same general procedure outlined above. However, continued STO growth did not require Sr-heavy cycling. A supercycle consistent with four Sr to three Ti subcycles (Sr:Ti cycle  $\approx$  4:3) at 225 °C yielded nearly stoichiometric film growth, consistent with our previous study.<sup>[40]</sup> Following the second growth step, the as-deposited STO films are amorphous to weakly crystalline. After completion of ALD growth, the STO films were annealed at 650 °C for 5 min to crystallize the deposited film fully on the STO seed layer.

Stoichiometric, crystalline STO films of up to 15-nm thick were produced using this two-step growth process. Thicker films may require more growth and anneal steps, or higher temperature growth to promote *in situ* crystallization. However, this method produces crystalline STO films in the appropriate thickness range (< 10 nm) for potential electronic applications, including high-mobility Ge-based transistors. Our expectation is that other crystalline oxides previously grown by ALD on single-crystal STO or STO-buffered Si (001) substrates can be monolithically integrated with Ge (001) by this growth technique.

## 3. Chemical and Structural Characterization

### 3.1. *In situ* X-ray Photoelectron Spectroscopy

The STO film and Ge-STO interface were analyzed using *in situ* x-ray photoelectron spectroscopy (XPS). After crystallization, the sample was transferred into the XPS analysis chamber. One of the keys to successful crystallization of the initial STO layer on Ge is ensuring that the film is stoichiometric to slightly Sr-rich. In addition, the presence of any amorphous layer (e.g., GeO<sub>2</sub>) prevents crystalline STO formation. Using *in situ* XPS, an optimized cycling ratio of two Sr cycles to one Ti cycle was found to produce stoichiometric to slightly Sr-rich ( $\approx$ 54%) films.

XPS analysis also verified that minimal, if any, GeO<sub>x</sub> formation is caused by the deposition of STO by ALD or the post-deposition annealing process. The presence of GeO<sub>x</sub> is generally identified by the chemical shifts ( $\Delta\epsilon$ ) of the Ge<sup>1+</sup> ( $\Delta\epsilon = 0.70 \pm 0.05$  eV), Ge<sup>2+</sup> ( $\Delta\epsilon = 1.70 \pm 0.10$  eV), Ge<sup>3+</sup> ( $\Delta\epsilon = 2.81 \pm 0.06$  eV), and Ge<sup>4+</sup> ( $\Delta\epsilon = 3.5 \pm 0.1$  eV) oxidation state components.<sup>[56]</sup> Deconvolution of the Ge 3d high-resolution spectrum was performed using CasaXPS as described in the Experimental Details to identify contributions of different Ge species after STO deposition and annealing, as shown in **Figure 3**. The spectrum is found to have contributions from bulk Ge (3d<sub>5/2</sub> and 3d<sub>3/2</sub> at 29.62 and 30.12 eV, respectively), an interfacial Ge species at lower binding energy (3d<sub>5/2</sub> and 3d<sub>3/2</sub> at 29.08 and 29.67 eV, respectively), and Ge<sub>2</sub>O (Ge<sup>1+</sup>) with 3d<sub>5/2</sub> and 3d<sub>3/2</sub> components at 30.28 and 30.91 eV, respectively. The exact bonding of the interfacial Ge species is not fully known, but appears similar to the shift that is observed for the Ge (001) surface dimerization.<sup>[57]</sup> It can be reasonably concluded that the interface is free of any further suboxides, namely, GeO (Ge<sup>2+</sup>), Ge<sub>2</sub>O<sub>3</sub> (Ge<sup>3+</sup>), or GeO<sub>2</sub> (Ge<sup>4+</sup>) species. As a comparison, deconvolution of the Ge

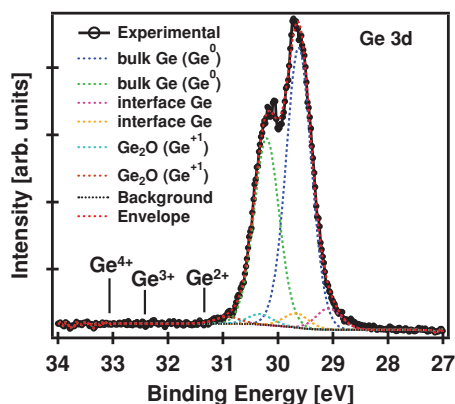


**Figure 3.** Spectral fitting of the high-resolution Ge 3d core-level spectrum after deposition of  $\approx 2$  nm STO and post-deposition annealing at 650 °C. The approximate positions of the Ge<sup>2+</sup>, Ge<sup>3+</sup>, and Ge<sup>4+</sup> oxidation state components are indicated.

3d high-resolution spectrum for the clean Ge (001) surface is provided in the Supporting Information. The Ge<sub>2</sub>O (Ge<sup>+1</sup>) component is estimated at 1.3% of the total Ge signal (Figure 3), which is comparable to the 0.8% contribution Ge<sub>2</sub>O makes to cleaned Ge (Supporting Information). Since the samples must be transferred from the annealing chamber into either the analytical or the ALD chambers it is not possible to establish if any, or additional, Ge<sub>2</sub>O forms during ALD and subsequent annealing of the STO layer.

Figure 4 shows XP spectra of an 8-nm thick STO sample grown on germanium. The XPS scans were taken before ALD growth, after 36 subcycles ( $\approx 2$  nm), and after 155 subcycles ( $\approx 8$  nm). The STO layer was crystallized each time by post-deposition vacuum annealing at 650 °C for 5 min. After cooling, the sample was moved to the XPS analysis chamber. Core levels of Ge 3d and O 1s are shown in Figure 4(a) and 4(b), respectively. The Ge 3d signal intensity decreases with the number of ALD cycles (thickness of STO film) and consistent with Figure 3, no GeO<sub>x</sub> ( $x \geq 1$ ) formation is observed. The Sr 3d and Ti 2p core levels shown in Figure 3(c) and 3(d) are consistent with fully oxidized species (Sr<sup>2+</sup> and Ti<sup>4+</sup>).

### 3.2. X-ray and Electron Diffraction

X-ray and electron diffraction techniques were used to confirm the crystalline structure, epitaxial relation, and thickness of the STO films. Evolution of the RHEED patterns from the Ge substrate to an 8-nm thick crystalline STO film is shown in Figure 5. The 2 $\times$ 1 surface reconstruction of the clean Ge surface after thermal deoxidation is shown in Figure 5(a). The intensity of the  $\frac{1}{2}$ -order spots are a strong indicator of the quality of the Ge (001) surface. After thermal deoxidation at 700 °C for 1 hr, a high-quality Ge (001) surface is achieved, provided that there is minimal residual carbon in the annealing chamber. The sample can then be transferred *in vacuo* to the ALD chamber. Deposition of the STO film occurs at a relatively low substrate temperature (225 °C), which results in the as-deposited film being amorphous to weakly crystalline. An example RHEED pattern of an 8-nm thick film, prior to crystallization, is shown in Figure 5(b).

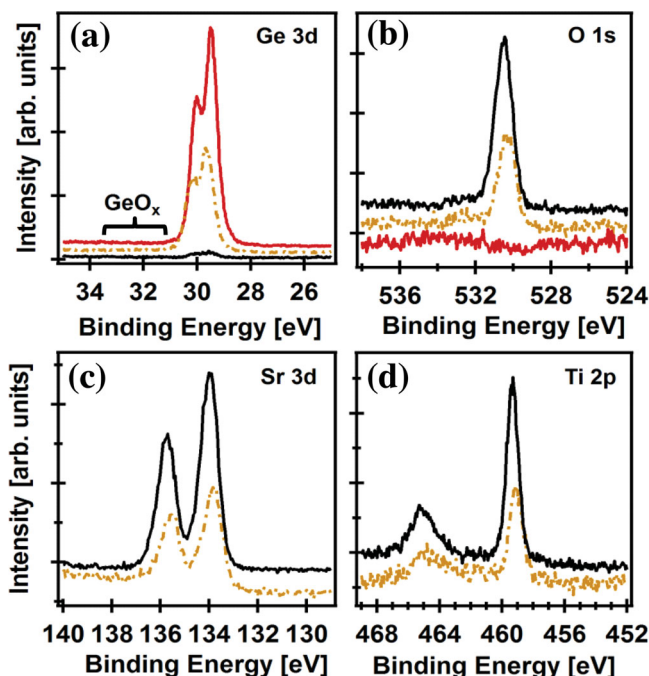


**Figure 4.** X-ray photoelectron spectra of the (a) Ge 3d, (b) O 1s, (c) Sr 3d, and (d) Ti 2p before ALD growth (solid red line), after 36 subcycles ( $\approx 2$  nm STO) (dashed brown line), and after 155 subcycles ( $\approx 8$  nm STO) (solid black line). The deposition temperature was 225 °C with a Sr:Ti sub-cycle ratio of 2:1 for the crystalline seed layer and 4:3 for the thicker STO film. (The intensity scaling of the spectra has been adjusted for clarity.)

Provided that the film is stoichiometric to slightly Sr-rich, post-deposition annealing at 650 °C for 5 min results in a crystalline film with epitaxial registry to the underlying Ge (001) substrate. The RHEED patterns for an 8-nm thick STO film grown on Ge (001) are shown in Figure 5(c) and 5(d). The images are taken along the [110] and [100] azimuth of STO, respectively. The streak patterns are comparable to that of STO films grown by molecular beam epitaxy, confirming the high degree of crystallinity for the ALD-grown film.

The structure of the STO film was confirmed by XRD to be consistent with the cubic perovskite, as shown in Figure 6.

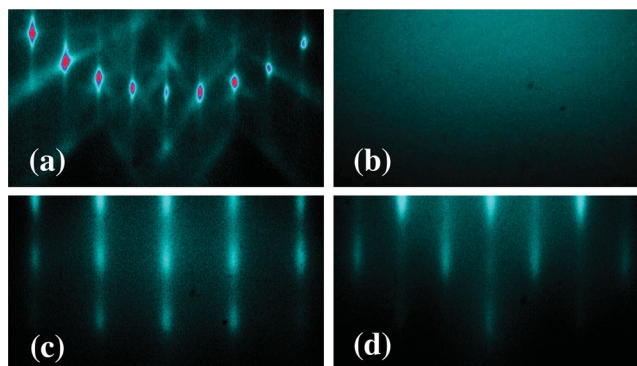


**Figure 5.** RHEED images of (a) clean Ge surface (before ALD growth), (b) after the second STO deposition (155 total subcycles), and [(c), (d)] after growth and annealing at 650 °C of an 8-nm thick STO film. The beam is aligned along the [110] and [100] azimuth for (c) and (d), respectively.

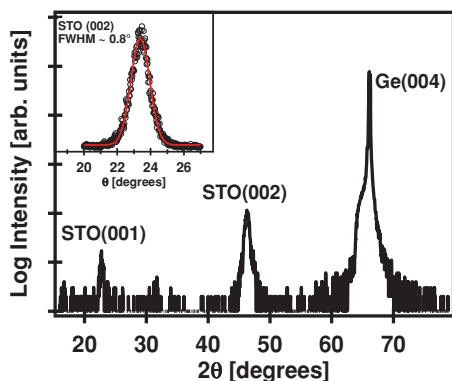


**Figure 6.** X-ray diffraction pattern for a 15-nm thick STO film grown by ALD on Ge (001) at 225 °C. (top left inset) Rocking curve around the STO (002) peak showing a FWHM of  $\approx 0.8^\circ$ . The sample was post-deposition annealed in vacuum at 600 °C for 5 min.

A rocking curve around the STO (002) peak gave a full-width half-maximum of  $\approx 0.8^\circ$  (Figure 6 inset), indicating a reasonable degree of out-of-plane orientation. The STO and Ge (001) substrate are epitaxially aligned such that  $(001)_{\text{STO}}(001)_{\text{Ge}}$  and  $(100)_{\text{STO}}(110)_{\text{Ge}}$ , leading to a  $45^\circ$  in-plane rotation that is expected for lattice-matching between the STO and Ge (001) substrate. From the bulk lattice constant for STO ( $a = 3.905 \text{ \AA}$ ) and the Ge (001) surface spacing along the [110] direction ( $3.992 \text{ \AA}$ ), the STO film is 2.1% tensile-strained when grown on Ge (001). Assuming STO is perfectly strained to Ge with a Poisson ratio of 0.232,<sup>[58]</sup> the STO (002) peak should be at  $46.73^\circ$ . Experimentally, XRD of an 8-nm thick STO film gave a peak position of  $46.75 \pm 0.05^\circ$ . However, thicker films relaxed to the nominal powder value ( $2\theta \approx 46.47^\circ$ ). Films greater than about 15 nm appear fully relaxed, with the STO (002) peak position at  $46.45 \pm 0.05^\circ$ .

High-resolution electron microscopy was used to examine cross-sections of the ALD-grown STO films. The cross-sectional TEM image (Figure 7) confirms the exceptional crystallinity of the STO film. There is an abrupt STO/Ge interface with no indication of an amorphous transition layer, in agreement with the XPS results. The selected-area electron diffraction pattern (Figure 7 inset) also confirms the excellent epitaxial registry between the two materials.

## 4. Electrical Characterization of SrTiO<sub>3</sub> and Al-doped SrTiO<sub>3</sub> Films

### 4.1. Dielectric Performance of Crystalline SrTiO<sub>3</sub> on Ge (001)

Electrical characterization of a 15-nm thick STO film was carried out by creating capacitor (metal-insulator-semiconductor) structures, as shown in Figure 8. Capacitance-voltage (CV) and current-voltage (IV) measurements were performed on a 50- $\mu\text{m}$  radius top electrode. Both CV and IV curves are shown in Figure 9, where the capacitance and current are normalized by the area of the contact pad. From the CV measurement shown in Figure 9(a), the capacitance of the structure is estimated to be  $5.3 \mu\text{F}/\text{cm}^2$ . This corresponds to a relatively high dielectric

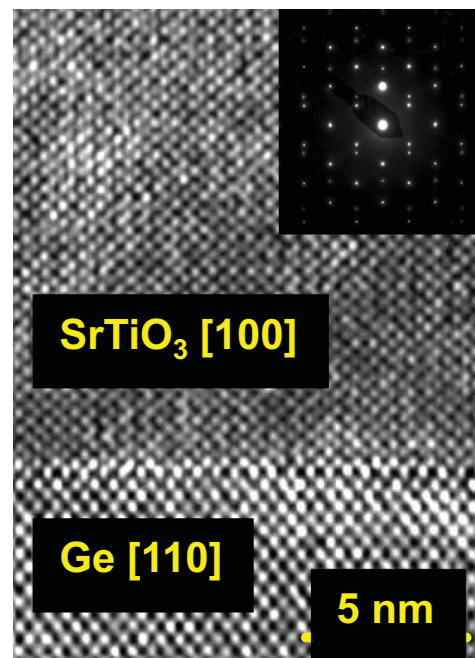


**Figure 7.** High-resolution transmission electron micrograph showing cross-section of a 15-nm thick STO film grown on Ge (001) by ALD. (top right inset) Selected-area electron diffraction pattern showing epitaxial registry between the substrate and film.

constant ( $k \approx 90$ ) for the STO thin film, with an equivalent oxide thickness less than 0.7 nm.

As shown in Figure 9(b), the leakage current density is relatively high  $\approx 10 \text{ A}/\text{cm}^2$  at +1 V (0.7 MV/cm) bias. The high leakage current is attributed to the small conduction band offset between STO and Ge, which we found experimentally to be  $0.12 \pm 0.1 \text{ eV}$  based on XPS measurements of shallow core-level and valence band spectra. More detailed analysis of the band offset measurements for the STO/Ge heterojunction is provided in the Supporting Information. The relatively small conduction band offset ( $\approx 0.12 \text{ eV}$ ) of the STO/Ge heterojunction makes undoped STO unsuitable as a high- $k$  dielectric for Ge-based transistors.

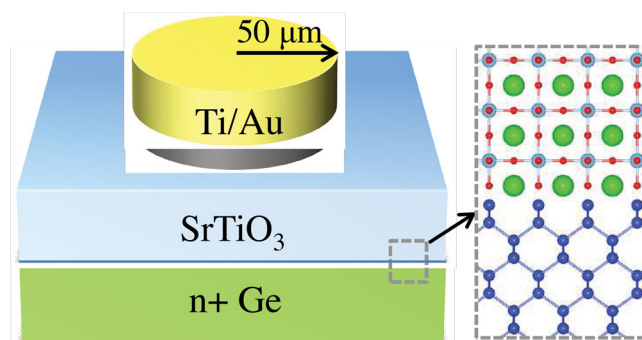


**Figure 8.** Schematic of the metal-insulator-semiconductor capacitor structure for crystalline STO grown on Ge (001) by ALD.

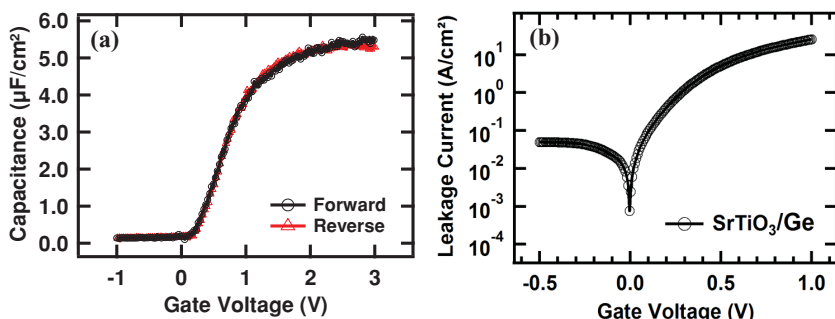


**Figure 9.** (a) Specific capacitance as a function of voltage bias for a 15-nm thick STO film grown on n+ Ge (001) by ALD, and (b) the gate leakage current density as a function of voltage bias measured from a typical Au(Ti)/STO/Ge structure.

#### 4.2. Improved Leakage Current of Al-doped SrTiO<sub>3</sub> Films

Different methods to reduce the leakage current of STO, such as inclusion of extra SrO layers and Al-doping of STO films, have been demonstrated previously.<sup>[30,59]</sup> By modifying our ALD cycle conditions to include an aluminum precursor, Al-doped STO films (SrTi<sub>1-x</sub>Al<sub>x</sub>O<sub>3-δ</sub>) were grown on the crystalline STO seed layer. The growth of the Al-doped STO films was similar to the growth of undoped STO, where some of the Ti subcycles were replaced with Al subcycles. Trimethyl aluminum (TMA) was used as the aluminum source. Several Al-doped STO films were grown with Al content varying between 8–13%. The films exhibited crystalline structure and quality similar to the undoped STO films using RHEED and XRD (not shown). The thicknesses of the Al-doped films were ≈8 nm, which includes the STO seed layer.

Electrical characterization of the Al-doped STO capacitor structures was carried out using a 50-μm radius top electrode. The leakage current density as a function of gate voltage is shown in **Figure 10**. Al-doped STO films of 8% and 13% show a leakage current density of ≈0.5 A/cm<sup>2</sup> and ≈0.1 A/cm<sup>2</sup>, respectively, for an applied field of 0.7 MV/cm. When compared to a 15-nm thick STO film, the leakage current density of an 8-nm thick Al-doped STO film with sufficient Al doping (≈13%) was two orders of magnitude lower. Considering the difference in thickness of the undoped and Al-doped films, the leakage

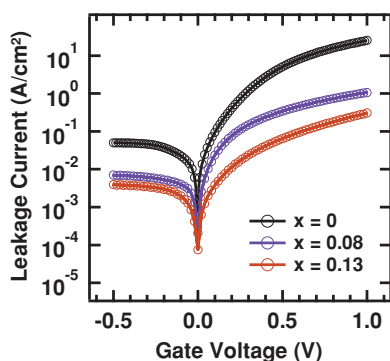


**Figure 10.** Gate leakage density as a function of voltage bias measured for Al-doped STO capacitor structures, Au(Ti)/SrTi<sub>1-x</sub>Al<sub>x</sub>O<sub>3-δ</sub>/Ge. The leakage current decreases with increasing aluminum content.

current reduction is significant. The decrease in leakage current is expected as a result of the band gap increase of ≈0.3 eV due to Al doping.<sup>[59]</sup> Similar band gap engineering concepts may be employed to further reduce the leakage current of high-*k* crystalline oxides grown by ALD on Ge.

#### 5. Concluding Remarks

We have grown crystalline SrTiO<sub>3</sub> (STO) directly on germanium via a purely chemical method, atomic layer deposition (ALD).

*In situ* x-ray photoelectron spectroscopy confirms the presence of stoichiometric STO

with no GeO<sub>x</sub> formation or carbon impurities observed. Epitaxial STO films up to 15-nm thick with a high-degree of crystallinity were grown on the Ge (001) substrate. The crystalline structure and orientation are confirmed via electron and x-ray diffraction. Capacitance-voltage and current-voltage measurements were performed on a 15-nm thick undoped STO film. The undoped STO showed a large dielectric constant of ≈90; however, the leakage current was unacceptably high (≈10 A/cm<sup>2</sup> at 0.7 MV/cm). To lower the leakage current, the STO films were doped with aluminum. An 8-nm thick Al-doped STO film showed a leakage current density ≈0.1 A/cm<sup>2</sup> at 0.7 MV/cm, roughly two orders of magnitude lower than the undoped STO.

Considering the wide-array of properties and lattice matching for perovskite oxides, this chemical growth technique has wide reaching potential for the monolithic integration of many functional oxides and heterostructures with semiconductor devices. The current work demonstrates the promise for ALD-grown crystalline oxides for advanced electronic applications in the near future, especially for high-mobility Ge-based transistors.

#### 6. Experimental Details

The as-received Ge wafer (provided by MTI Corp.) is diced into approximately 18 × 20 mm<sup>2</sup> sample sizes. Before loading into the UHV system, the sample is degreased by placing the wafer in ultrasonic baths of acetone, isopropyl alcohol, and water for 10 min each. The sample is then dried with nitrogen and exposed to ultraviolet/ozone for 15 min to remove residual carbon contamination. The sample is immediately loaded into the load lock chamber and pumped by a turbomolecular pump to a vacuum below 5 × 10<sup>-7</sup> torr before transferring into the annealing chamber. The sample is annealed at 700 °C in vacuum for 1 hr, and then lowered to 200 °C before transfer to the ALD system. The heating and cooling rates were fixed at 20 °C min<sup>-1</sup>.

The ALD system consists of a custom-built, hot-wall stainless steel rectangular chamber that is approximately 20-cm long, with a reactor volume of 460 cm<sup>3</sup>, as described in more detail elsewhere.<sup>[60]</sup> After loading the substrate into the ALD chamber, the reactor temperature is allowed to equilibrate for at least 30 min. Ultra-high purity argon is used as both the carrier and purge gas. Under deposition conditions, the argon is flowed into the ALD chamber, which is continuously pumped by a dual-stage rotary vane pump with a peak pumping speed of 6 ft<sup>3</sup> min<sup>-1</sup>. This maintains the ALD operating pressure at ≈1 torr. HyperSr and TTIP were vaporized at 130 °C and 40 °C, respectively, and water was held at room temperature (26 °C). The water dosing was regulated using an in-line needle valve.

XPS was performed using a VG Scienta R3000 analyzer and a monochromated Al K $\alpha$  source at 1486.6 eV. The analyzer is calibrated using a silver foil, where the Ag 3d<sub>5/2</sub> core level is defined to be 368.28 eV and the Fermi level of Ag at 0.00 eV. High-resolution spectra of the Sr 3d, Ti 2p, O 1s, C 1s, and Ge 3d core levels are measured using a pass energy of 100 eV with an analyzer slit width of 0.4 mm. Each high-resolution scan is measured four times and summed, using 50 meV steps with a dwell time of 157 ms per step. Film composition was estimated using CasaXPS (ver. 2.3.16) peak fitting, where the integrated intensities are divided by the Wagner relative sensitivity factors after a Shirley background subtraction.<sup>[61]</sup> Additionally, a thickness dependent energy exponent between 0 and 0.78 is used to account for kinetic energy variation with sampling depth.<sup>[62]</sup> The maximum exponent value (0.78) was calibrated using an STO single crystal substrate (MTI Corp.) where the Sr:Ti ratio was assumed to be 1:1.

RHEED patterns were obtained with an electron energy of 21 keV at a glancing angle of  $\approx 3^\circ$ . X-ray diffraction (XRD), x-ray reflectivity (XRR), rocking curve analysis, and off-axis phi scans were all conducted using a Bruker-AXS D8 Advance Powder Diffractometer using a sealed tube Cu K $\alpha$  radiation. Cross-sectional transmission electron microscopy (TEM) was performed with a 400-keV high-resolution electron microscope (JEM-4000EX) equipped with a double-tilt specimen holder. The sample was prepared using standard mechanical polishing followed by argon-ion-milling to perforation.

Capacitance-voltage (CV) and current-voltage (IV) measurements were performed on several undoped and Al-doped STO films grown by ALD on heavily doped n-type Ge ( $\rho \approx 0.04 \Omega\text{-cm}$ ). The STO films were annealed in air at 300 °C for 30 min prior to electrode deposition. The top electrode (50  $\mu\text{m}$  radius) on the STO surface was formed by photolithography, e-beam evaporation of 20-nm Ti followed by 160-nm Au, and lift-off. The Ge substrate was coated with Ti/Au as a bottom electrode. Both CV and IV were measured in air at room temperature by an Agilent 4156A precision semiconductor parameter analyzer. The sweeping voltage was applied to the top electrode with the bottom electrode grounded.

## Supporting Information

Supporting Information is available from the Wiley Online Library or from the author.

## Acknowledgements

This work was supported by the National Science Foundation (Award DMR-1207342), the Office of Naval Research (Grant N00014-10-10489), and the Air Force Office of Scientific Research (Grant FA9550-12-10494). Part of this work was supported by the Judson S. Swearingen Regents Chair in Engineering at the University of Texas at Austin. We acknowledge use of the facilities in the John M. Cowley Center for High Resolution Electron Microscopy at Arizona State University.

Received: February 7, 2014

Revised: April 10, 2014

Published online:

- [1] R. McKee, F. Walker, M. Chisholm, *Phys. Rev. Lett.* **1998**, *81*, 3014.
- [2] R. Droopad, Z. Yu, H. Li, Y. Liang, C. Overgaard, A. Demkov, X. Zhang, K. Moore, K. Eisenbeiser, M. Hu, J. Curless, J. Finder, *J. Cryst. Growth* **2003**, *251*, 638.
- [3] M. Sousa, C. Rossel, C. Marchiori, H. Siegwart, D. Caimi, J. P. Locquet, D. J. Webb, R. Germann, J. Fompeyrine, K. Babich, J. W. Seo, C. Dieker, *J. Appl. Phys.* **2007**, *102*, 104103.
- [4] J. W. Reiner, A. M. Kolpak, Y. Segal, K. F. Garrity, S. Ismail-Beigi, C. H. Ahn, F. J. Walker, *Adv. Mater.* **2010**, *22*, 2919.

- [5] A. A. Demkov, A. B. Posadas, H. Seo, M. Choi, K. J. Kormondy, P. Ponath, R. C. Hatch, M. D. McDaniel, T. Q. Ngo, J. G. Ekerdt, *ECS Trans.* **2013**, *54*, 255.
- [6] M. P. Warusawithana, C. Cen, C. R. Sleasman, J. C. Woicik, Y. Li, L. F. Kourkoutis, J. A. Klug, H. Li, P. Ryan, L. P. Wang, M. Bedzyk, D. A. Muller, L. Q. Chen, J. Levy, D. G. Schlom, *Science* **2009**, *324*, 367.
- [7] G. Niu, B. Vilquin, J. Penuelas, C. Botella, G. Hollinger, G. Saint-Girons, *J. Vac. Sci. Technol. B* **2011**, *29*, 041207.
- [8] Z. Yu, Y. Liang, C. Overgaard, X. Hu, J. Curless, H. Li, Y. Wei, B. Craigo, D. Jordan, R. Droopad, J. Finder, K. Eisenbeiser, D. Marshall, K. Moore, J. Kulik, P. Fejes, *Thin Solid Films* **2004**, *462–463*, 51.
- [9] X. Gu, D. Lubyshev, J. Batzel, J. M. Fastenau, W. K. Liu, R. Pelzel, J. F. Magana, Q. Ma, L. P. Wang, P. Zhang, V. R. Rao, *J. Vac. Sci. Technol. B* **2009**, *27*, 1195.
- [10] S. H. Baek, C. B. Eom, *Acta Materialia* **2013**, *61*, 2734.
- [11] I. Vrejoiu, M. Alexe, D. Hesse, U. Gösele, *Adv. Funct. Mater.* **2008**, *18*, 3892.
- [12] K. J. Jin, H. B. Lu, K. Zhao, C. Ge, M. He, G. Z. Yang, *Adv. Mater.* **2009**, *21*, 4636.
- [13] R. Ramesh, N. A. Spaldin, *Nat. Mater.* **2007**, *6*, 21.
- [14] J. Mannhart, D. G. Schlom, *Science* **2010**, *327*, 1607.
- [15] H. W. Jang, D. A. Felker, C. W. Bark, Y. Wang, M. K. Niranjan, C. T. Nelson, Y. Zhang, D. Su, C. M. Folkman, S. H. Baek, S. Lee, K. Janicka, Y. Zhu, X. Q. Pan, D. D. Fong, E. Y. Tsymbal, M. S. Rzechowski, C. B. Eom, *Science* **2011**, *331*, 886.
- [16] H. Y. Hwang, Y. Iwasa, M. Kawasaki, B. Keimer, N. Nagaosa, Y. Tokura, *Nat. Mater.* **2012**, *11*, 103.
- [17] S. Stemmer, A. J. Millis, *MRS Bull.* **2013**, *38*, 1032.
- [18] M. Leskelä, M. Ritala, *Thin Solid Films* **2002**, *409*, 138.
- [19] S. M. George, *Chem. Rev.* **2010**, *110*, 111.
- [20] D. A. Muller, T. Sorsch, S. Moccio, F. H. Baumann, K. Evans-Lutterodt, G. Timp, *Nature* **1999**, *399*, 758.
- [21] R. Chau, S. Datta, M. Doczy, J. Kavalieros, M. Metz, in *Extended Abstracts of Int. Workshop on Gate Insulator*, Tokyo, Japan **2003**, pp. 124–126.
- [22] M. V. Fischetti, S. E. Laux, *J. Appl. Phys.* **1996**, *80*, 2234.
- [23] Front End Processes Chapter, in *International Roadmap for Semiconductors (2012 Edition)*, www.itrs.net, accessed January 2014.
- [24] Y. Kamata, *Materials Today* **2008**, *11*, 30.
- [25] R. M. Wallace, P. C. McIntyre, J. Kim, Y. Nishi, *MRS Bull.* **2009**, *34*, 493.
- [26] C. Claeys, E. Simoen, *Germanium-Based Technologies: From Materials to Devices*, Elsevier, Kidlington, Oxford, UK **2007**.
- [27] K. Kita, T. Takahashi, H. Nomura, S. Suzuki, T. Nishimura, A. Toriumi, *Appl. Surf. Sci.* **2008**, *254*, 6100.
- [28] M. Caymax, M. Houssa, G. Pourtois, F. Bellenger, K. Martens, A. Delabie, S. Van Elshocht, *Appl. Surf. Sci.* **2008**, *254*, 6094.
- [29] I. K. Oh, M. K. Kim, J. S. Lee, C. W. Lee, C. Lansalot-Matras, W. Noh, J. Park, A. Noori, D. Thompson, S. Chu, W. J. Maeng, H. Kim, *Appl. Surf. Sci.* **2013**, *287*, 349.
- [30] R. A. McKee, F. J. Walker, M. F. Chisholm, *Science* **2001**, *293*, 468.
- [31] A. Lin, X. Hong, V. Wood, A. A. Verevkin, C. H. Ahn, R. A. McKee, F. J. Walker, E. D. Specht, *Appl. Phys. Lett.* **2001**, *78*, 2034.
- [32] B. T. Liu, K. Maki, Y. So, V. Nagarajan, R. Ramesh, J. Lettieri, J. H. Haeni, D. G. Schlom, W. Tian, X. Q. Pan, F. J. Walker, R. A. McKee, *Appl. Phys. Lett.* **2002**, *80*, 4801.
- [33] J. Wang, H. Zheng, Z. Ma, S. Prasertchoung, M. Wuttig, R. Droopad, J. Yu, K. Eisenbeiser, R. Ramesh, *Appl. Phys. Lett.* **2004**, *85*, 2574.
- [34] V. Vaithyanathan, J. Lettieri, W. Tian, A. Sharan, A. Vasudevarao, Y. L. Li, A. Kochhar, H. Ma, J. Levy, P. Zschack, J. C. Woicik, L. Q. Chen, V. Gopalan, D. G. Schlom, *J. Appl. Phys.* **2006**, *100*, 024108.
- [35] A. K. Pradhan, J. B. Dadson, D. Hunter, K. Zhang, S. Mohanty, E. M. Jackson, B. Lasley-Hunter, K. Lord, T. M. Williams, R. R. Rakhimov, J. Zhang, D. J. Sellmyer, K. Inaba, T. Hasegawa,

- S. Mathews, B. Joseph, B. R. Sekhar, U. N. Roy, Y. Cui, A. Burger, *J. Appl. Phys.* **2006**, *100*, 033903.
- [36] J. W. Reiner, A. Posadas, M. Wang, M. Sidorov, Z. Krivokapic, F. J. Walker, T. P. Ma, C. H. Ahn, *J. Appl. Phys.* **2009**, *105*, 124501.
- [37] A. Posadas, M. Berg, H. Seo, A. de Lozanne, A. A. Demkov, D. J. Smith, A. P. Kirk, D. Zhernokletov, R. M. Wallace, *Appl. Phys. Lett.* **2011**, *98*, 053104.
- [38] H. Seo, A. B. Posadas, C. Mitra, J. Ramdani, A. V. Kvit, A. A. Demkov, *Phys. Rev. B* **2012**, *86*, 075301.
- [39] M. D. McDaniel, A. Posadas, T. Q. Ngo, A. Dhamdhere, D. J. Smith, A. A. Demkov, J. G. Ekerdt, *J. Vac. Sci. Technol. B* **2012**, *30*, 04E111.
- [40] M. D. McDaniel, A. Posadas, T. Q. Ngo, A. Dhamdhere, D. J. Smith, A. A. Demkov, J. G. Ekerdt, *J. Vac. Sci. Technol. A* **2013**, *31*, 01A136.
- [41] T. Q. Ngo, A. B. Posadas, M. D. McDaniel, C. Hu, J. Bruley, E. T. Yu, A. A. Demkov, J. G. Ekerdt, *Appl. Phys. Lett.* **2014**, *104*, 082910.
- [42] T. Q. Ngo, A. Posadas, M. D. McDaniel, D. A. Ferrer, J. Bruley, C. Breslin, A. A. Demkov, J. G. Ekerdt, *J. Cryst. Growth* **2013**, *363*, 150.
- [43] P. Ponath, A. B. Posadas, R. C. Hatch, A. A. Demkov, *J. Vac. Sci. Technol. B* **2013**, *31*, 031201.
- [44] Manufactured and supplied by Air Liquide.
- [45] Supplied by Sigma-Aldrich (99.999%).
- [46] M. Ritala, M. Leskela, L. Niinistö, P. Haussalo, *Chem. Mater.* **1993**, *5*, 1174.
- [47] M. Vehkamäki, T. Hatanpää, T. Hänninen, M. Ritala, M. Leskelä, *Electrochem. Solid-State Lett.* **1999**, *2*, 504.
- [48] J. Aarik, A. Aidla, T. Uustare, M. Ritala, M. Leskelä, *Appl. Surf. Sci.* **2000**, *161*, 385.
- [49] M. Vehkamäki, T. Hänninen, M. Ritala, M. Leskelä, T. Sajavaara, E. Rauhala, J. Keinonen, *Chem. Vap. Deposition* **2001**, *7*, 75.
- [50] R. Katamreddy, V. Omarjee, B. Feist, C. Dussarrat, M. Singh, C. Takoudis, *ECS Trans.* **2008**, *16*, 487.
- [51] R. Katamreddy, Z. Wang, V. Omarjee, P. V. Rao, C. Dussarrat, N. Blasco, *ECS Trans.* **2009**, *25*, 217.
- [52] B. G. Willis, C. B. Zhang, *ECS Trans.* **2010**, *33*, 51.
- [53] C. B. Zhang, L. Wielunski, B. G. Willis, *Appl. Surf. Sci.* **2011**, *257*, 4826.
- [54] S. W. Lee, J. H. Han, S. Han, W. Lee, J. H. Jang, M. Seo, S. K. Kim, C. Dussarrat, J. Gatineau, Y. S. Min, C. S. Hwang, *Chem. Mater.* **2011**, *23*, 2227.
- [55] W. Lee, J. H. Han, W. Jeon, Y. W. Yoo, S. W. Lee, S. K. Kim, C. H. Ko, C. Lansalot-Matras, C. S. Hwang, *Chem. Mater.* **2013**, *25*, 953.
- [56] A. Molle, M. N. K. Bhuiyan, G. Tallarida, M. Fanciulli, *Appl. Phys. Lett.* **2006**, *89*, 083504.
- [57] P. E. J. Eriksson, R. I. G. Uhrberg, *Phys. Rev. B* **2010**, *81*, 125443.
- [58] H. Ledbetter, M. Lei, S. Kim, *Phase Transit.* **1990**, *23*, 61.
- [59] A. B. Posadas, C. Lin, A. A. Demkov, S. Zollner, *Appl. Phys. Lett.* **2013**, *103*, 142906.
- [60] M. D. McDaniel, A. Posadas, T. Wang, A. A. Demkov, J. G. Ekerdt, *Thin Solid Films* **2012**, *520*, 6525.
- [61] C. D. Wagner, *J. Electron Spectrosc. Relat. Phenom.* **1983**, *32*, 99.
- [62] C. D. Wagner, L. E. Davis, W. M. Riggs, *Surf. Interface Anal.* **1980**, *2*, 53.